Green Chemistry

PAPER

View Article Online
View Journal

Cite this: DOI: 10.1039/d6gc02101h

Precursor-regulated reconstruction of Cu-based catalysts for efficient electrocatalytic urea synthesis from CO_2 and nitrate

Ke Wu,[a] Guojie Ye,[a] Zhengwei Zhou,[a] Zuofeng Chen,[b] Zhendong Lei[a] and Deli Wu *[a]

Electrocatalytic urea synthesis from CO_2 and nitrate provides a sustainable route for coupling carbon utilization with nitrogen-waste upgrading under mild conditions. However, achieving scalable urea yields remains challenging due to the difficulty of synchronizing carbon- and nitrogen-containing intermediates on catalyst surfaces, particularly under practical conditions. Although Cu-based catalysts have been widely studied for C–N coupling, how precursor chemistry regulates their working-state reconstruction during electrolysis is still not well understood. Here, we systematically prepared two Cu-based catalysts enriched with basic surface groups (CO_3^{2-}/OH^-), $Cu_2(OH)_2CO_3$ and $Cu(OH)_2$, and investigated their nanoscale reconstruction pathways during electrocatalytic C–N coupling for urea synthesis. Hierarchically structured $Cu_2(OH)_2CO_3$ delivered a urea yield of 63.20 mmol h^{-1} $g_{cat.}^{-1}$ with a faradaic efficiency of 16.21% at −0.9 V *versus* RHE, nearly twice that of $Cu(OH)_2$. Quasi-*in situ* X-ray photoelectron spectroscopy and X-ray absorption spectroscopy revealed that $Cu_2(OH)_2CO_3$ follows a carbonate-regulated reconstruction distinct from that of $Cu(OH)_2$ and maintains a broader mixed-valence working-state window composed of Cu^{2+}, Cu^+, and Cu^0 during catalysis. *In situ* FTIR spectroscopy and density functional theory calculations further support a pathway in which CO_2 is reduced to *CO on Cu^+ sites, nitrate is reduced to $*NH_2$ on Cu^0 sites, and their interfacial coupling leads to urea formation. Furthermore, we validated the feasibility of $Cu_2(OH)_2CO_3$ for electrocatalytic C–N coupling in an environmental scenario of food waste biological treatment. This work elucidates precursor-regulated reconstruction as an effective design principle for promoting selective C–N coupling and advancing more sustainable urea electrosynthesis in complex waste-derived environments.

Received 8th April 2026,
Accepted 21st May 2026

DOI: 10.1039/d6gc02101h

rsc.li/greenchem

Green foundation

1. The work introduces a precursor-regulated reconstruction strategy for electrocatalytic urea synthesis from CO_2 and nitrate, demonstrating that simple Cu precursors can be used to couple carbon utilization with nitrate remediation under ambient conditions and thereby provide a waste-to-value alternative to conventional energy-intensive urea production.

2. We demonstrated that simple Cu precursor chemistry can regulate catalyst restructuring and construct a mixed-valent working interface without the need for precious metals or complex catalyst designs. $Cu_2(OH)_2CO_3$ achieved a urea yield of 63.20 mmol h^{-1} $g_{cat.}^{-1}$ and a faradaic efficiency of 16.21% at −0.9 V (*vs.* RHE) and enabled the electrosynthesis of urea in food waste leachate.

3. Future research will be dedicated to expanding the utilization of precursor-regulated dynamic interfaces in different electrocatalytic C–N coupling processes using advanced electrolyzer designs to further improve faradaic efficiency and minimize overall energy consumption.

[a]*State Key Laboratory of Water Pollution Control and Green Resource Recycling, College of Environmental Science & Engineering, Key Laboratory of Water Supply, Water Saving and Ecological Governance in the Yangtze River Delta, Ministry of Water Resources, Shanghai Institute of Pollution Control and Ecological Security, Tongji University, Shanghai 200092, China. E-mail: wudeli@tongji.edu.cn, wuke@tongji.edu.cn, yeguojie@tongji.edu.cn, 2210532@tongji.edu.cn, leizd95@tongji.edu.cn; Fax: +86-21-65983602*

[b]*Shanghai Key Laboratory of Chemical Assessment and Sustainability, School of Chemical Science and Engineering, Tongji University, Shanghai 200092, China. E-mail: zfchen@tongji.edu.cn*

1. Introduction

With the continued increase in anthropogenic carbon emissions and the ongoing accumulation of inorganic reactive nitrogen in water systems, the concentrations of CO_2 in the atmosphere and nitrate (NO_3^-) in water bodies have risen to levels that pose a threat to the human environment.[1,2] According to statistics, global annual anthropogenic CO_2 emissions have reached 40 Gt. Without substantive control and

mitigation measures, global average surface temperatures are projected to rise by 2.7–3 °C or more by the end of this century compared to the late 19th century.[3] Meanwhile, NO_3^- finds its way into wastewater *via* excessive fertilization and industrial discharges disrupt the global nitrogen cycle and pose a threat to the environment and public health.[4] The conventional method for removing NO_3^- from wastewater involves converting it into N_2 through denitrification, a process that is energy-intensive and generates additional carbon emissions.[5] Therefore, utilizing renewable electricity to convert CO_2 and NO_3^- into the high-value chemical urea represents a promising "turning waste into treasure" strategy. This process enables the direct formation of C–N bonds under mild conditions, simultaneously achieving carbon resource utilization and the conversion of nitrogen-containing pollutants.

Urea ($CO(NH_2)_2$) is the most widely used nitrogen fertilizer, with a nitrogen content of up to approximately 46%. It plays a critical role in agriculture and population growth and is also widely used in the production of dyes, resins, and pharmaceuticals.[6] To date, the industrial production of urea heavily relies on high temperatures and pressures.[7] Specifically, the Haber–Bosch process for synthesizing one of its feedstocks, NH_3, consumes approximately 2% of global energy demand and accounts for 1.44% of global CO_2 emissions.[8,9] In contrast, electrochemical C–N coupling technology eliminates the need for the separate production, transportation, and storage of NH_3, enabling the direct, one-step production of urea from carbon- and nitrogen-containing feedstocks at ambient temperature and pressure. Electrocatalytic C–N coupling can reduce the global carbon footprint, maintain nitrogen balance and transform the urea industry.

A wide variety of catalysts have been developed for the electrosynthesis of urea through C–N coupling, including single-atom catalysts,[10,11] vacancy defect engineering,[12,13] crystal surface modulation,[14,15] alloying[16,17] and heteroatom doping.[18] However, electrocatalytic urea synthesis involves a multistep electrochemical process (proton-coupled electron transfer, PCET) and chemical processes (C–N coupling).[19–21] The formidable challenge lies in identifying the key reactive sites, where parallel CO_2RR and NO_3RR, as well as the unavoidable hydrogen evolution reaction (HER) at negative potentials, strongly compete with the desired urea formation, resulting in complex product distributions and low urea yields.[22,23] Recent advances in electrocatalytic urea synthesis from CO_2 and nitrate have demonstrated that interfacial coordination and molecular/interface engineering are effective strategies for regulating key adsorbed intermediates.[24,25] For example, molecularly engineered Ni–O–C interfacial sites on g-C_3N_4 have been reported to promote urea electrosynthesis by tuning the interfacial coordination environment for CO_2/NO_3^- co-reduction.[24] Therefore, it is necessary to design a catalyst that not only enables the co-activation and reaction of the reactants but also optimizes the adsorption of intermediate species, constructs efficient sites conducive to C–N coupling, and reduces the occurrence of side reactions. Also, an additional requirement is that such catalytic systems should rely on simple, readily accessible materials and remain effective in chemically complex, waste-derived environments rather than only in idealized electrolytes.

Cu-based catalysts have been extensively utilized and studied in the CO_2RR and NO_3RR.[26,27] They possess the ability to convert CO_2 into C_{2+} products with high activity and selectivity.[28–30] Additionally, they have been demonstrated to convert NO_3^- into NH_3 with a Faraday efficiency exceeding 90%.[31,32] Cu catalysts often undergo significant electrochemical restructuring during the reaction, forming a non-equilibrium active surface state characterized by mixed valence states, altered local coordination environments, and newly exposed low-coordination sites.[33,34] Precursor-dependent evolution of derived Cu catalysts has been shown to regulate defect density, strain, interfacial species, and adsorbate stabilization.[35] Compared to oxide-derived Cu catalysts such as CuO/Cu_2O, carbonate- and hydroxide-derived Cu-based catalysts naturally possess basic surface groups (CO_3^{2-}/OH^-) and oxygen-rich coordination environments. These characteristics may facilitate CO_2 adsorption, stabilize interfacial intermediates, and suppress the side reaction of the HER.[36,37] Related studies on CO_2 electro-reduction have also shown that surface hydroxyl species can increase the residence time of *CO on the Cu surface and lower the energy barrier for subsequent coupling reactions.[38] However, current research on the electrosynthesis of urea on Cu substrates has largely emphasized enhancing catalytic performance or a specific C–N coupling pathway, while neglecting whether the precursor chemistry can encode nanoscale restructuring trajectories and further govern the formation and maintenance of mixed-valent interfacial regions under operating conditions.

Here, we synthesized two Cu-based catalysts—$Cu_2(OH)_2CO_3$ and $Cu(OH)_2$—which have different precursor anions for the electrochemical synthesis of urea from CO_2 and NO_3^-. $Cu_2(OH)_2CO_3$ forms hierarchical flower-like assemblies built from nanoscale subunits, whereas $Cu(OH)_2$ exhibits a rod-dominated morphology. More importantly, *in situ* and quasi-*in situ* characterization studies reveal that $Cu_2(OH)_2CO_3$ follows a distinct nanoscale reconstruction trajectory and maintains a broader Cu^{2+}–Cu^+–Cu^0 working-state ensemble under electroreduction conditions (Fig. 1). This reconstructed state is more favorable for stabilizing *CO and synchronizing its temporal coexistence with nitrogenous intermediates, leading to a urea yield rate of 63.20 mmol h^{-1} $g_{cat.}^{-1}$ and a faradaic efficiency of 16.21% at −0.9 V *versus* RHE. Density functional theory calculations further suggest that Cu^+ sites favor carbon activation to *CO, whereas adjacent Cu^0 sites facilitate nitrate reduction to *NH_2, making their subsequent coupling more accessible within the reconstructed mixed-valence environment. More importantly, the $Cu_2(OH)_2CO_3$ catalyst also exhibits strong matrix tolerance in food-waste leachate, enabling continuous urea electrosynthesis in a real waste-derived medium. By linking precursor chemistry, dynamic active-state evolution, and operation in a complex environmental matrix, this work establishes a practical design principle for more sustainable electrocatalytic C–N coupling.

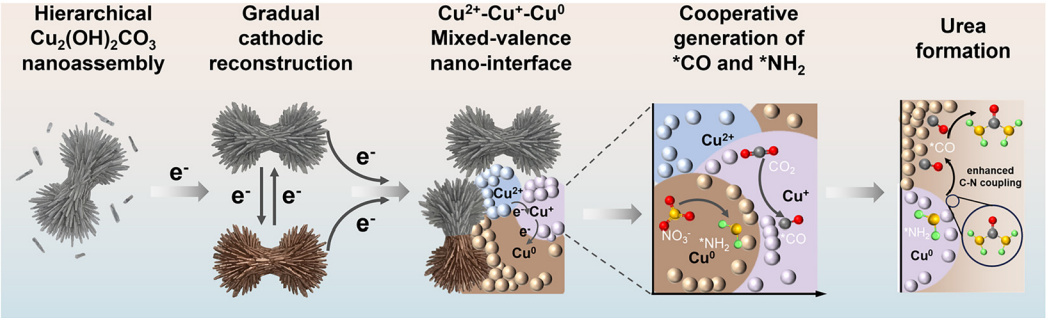

Fig. 1 Schematic illustration of the precursor-regulated reconstruction pathway of $Cu_2(OH)_2CO_3$ for electrocatalytic urea synthesis.

2. Experimental details

2.1. Synthesis of $Cu_2(OH)_2CO_3$

A simple synthesis method of $Cu_2(OH)_2CO_3$ was developed. Specifically, $Cu(NO_3)_2{\cdot}3H_2O$ (750 mg) was ultrasonically dissolved in 20 mL DIW for 20 min (Solution A). Na_2CO_3 (400 mg) was dissolved in 10 mL of DIW (Solution B). Solution B was added dropwise into Solution A under stirring. The mixture was stirred for 1 h. The obtained precipitate was washed and dried under vacuum at 40 °C. Finally, the precipitate was heated in a furnace at 150 °C for 1 h (5 °C min^{-1}) under an Ar flow to obtain $Cu_2(OH)_2CO_3$.

2.2. Synthesis of $Cu(OH)_2$

First, 50 mL of 0.05 M aqueous solution of $Cu(NO_3)_2{\cdot}3H_2O$ was prepared at room temperature. Subsequently, 1 mL of 25% ammonia solution was slowly added into the solution, followed by 1 mL of 0.01 M NaOH aqueous solution under stirring. The mixture was heated to 60 °C for 15 min and then cooled to room temperature. Then, the mixture was subjected to centrifugation and copious washing with water to a neutral pH to obtain the resulting bluish $Cu(OH)_2$ nanocrystals. The final product was dried in a vacuum oven overnight at 30 °C.

2.3. Materials characterization

The SEM images and energy dispersive X-ray spectroscopy (EDS) elemental maps were obtained from a ZEISS GeminiSEM 300 scanning electron microscope. Trace samples were taken and glued directly onto conductive adhesive and sprayed with gold for 45 s using a Quorum SC7620 sputter coater. HRTEM was acquired with the Japanese JEOL JEM-F200. The sample was dispersed into ethanol solution for ultrasound and dripped on the copper grid for observation. X-ray diffraction (XRD) was performed using a Rigaku D/max 2200PC with a Cu Kα source. Diffraction patterns from 10° to 80° were collected at a scan speed of 5° min^{-1}. X-ray photoelectron spectrum (XPS) analysis was performed on the Thermo Scientific K-Alpha system using monochromatic Al Kα radiation. The sample was cut into 0.5 × 0.5 cm^2.

2.4. XPS and XANES measurements after electrolysis

$Cu_2(OH)_2CO_3$ and $Cu(OH)_2$ electrodes were electrolyzed for 15, 30 and 60 min in 0.1 M $KHCO_3$ + 0.05 M KNO_3 under −0.9 V (*versus* RHE) conditions with carbon dioxide bubbles (20 mL min^{-1}). Immediately after the test, the electrodes were washed with DIW and vacuum dried (20 °C). Ar-protected samples were transferred to a sealed chamber filled with Ar for storage. Samples unprotected by Ar were exposed to air for 1 h. The samples were then XPS and XANES tested together.

2.5. Electrochemical in situ ATR-FTIR measurement

Electrochemical *in situ* FTIR measurements were performed with the Thermo Scientific Nicolet iS50 FTIR spectrometer using a monocrystalline silicon ingot substrate with a gold-plated surface for signal surface enhancement. The counter electrodes and reference electrodes were Pt foil and RHE electrodes, respectively. The scanning range was 4000–1000 cm^{-1}. Each infrared absorption spectrum was acquired by averaging 32 scans at a resolution of 4 cm^{-1}. The background spectrum of the catalyst electrode was acquired at an open-circuit voltage before each systemic measurement, and the measured potential ranges of the electrocoupling reaction were −0.4 V to −1.1 V *versus* RHE with an interval of 0.1 V.

2.6. Electrochemical procedure

The electrochemical experiments were conducted on a CHI 760D electrochemical workstation by using a three-electrode configuration with an H-cell (working electrode, Pt foil as the counter electrode and Ag/AgCl/saturated KCl as the reference electrode). The pretreated Nafion 117 membrane (DuPont) acts as the separator. Before tests, the Nafion 117 membrane was pretreated by heating it in H_2O_2 (5%) aqueous solution at 80 °C for 1 h and ultrapure water at 80 °C for another 1 h, respectively, followed by treatment in 0.05 M H_2SO_4 for 1 h and ultrapure water for another 3 h. The electrolyte utilized for coupling reactions was CO_2-saturated 0.1 M $KHCO_3$ with 0.05 M KNO_3. Experiments were performed after adjusting the pH to 10 using 2 M KOH.

Before electrochemical tests, the cathode electrolyte was purged with CO_2 at a flow rate of 50 mL min^{-1} for 30 min. Then, the feeding gas of CO_2 was controlled at 20 mL min^{-1}, where CO_2, NO_3^-, and protons combined with electrons to form the urea product. Controlled potential electrolysis was performed at each potential for 1.0 h. The electrocatalytic CO_2 reduction reaction was carried out in CO_2-saturated 0.1 M

$KHCO_3$. The electrocatalytic NO_3^- reduction reaction was performed in an Ar-saturated mixture of 0.1 M $KHCO_3$ and 0.05 M KNO_3.

2.7. Cathode preparation

2 mg of electrocatalyst was dispersed in 950 μL of a mixture of isopropanol and water (isopropanol : water = 2 : 1) and 50 μL of Nafion, followed by sonication for 40 min to form a homogeneous ink. Then, 50 μL of catalyst ink was loaded onto carbon paper and dried naturally to obtain the working electrode. The geometric area of the working electrode was 1.0 × 1.0 cm^2, and the catalyst loading was 0.1 mg cm^{-2}. The applied potentials were measured against the Ag/AgCl reference electrode and converted into the RHE reference scale using $E_{RHE} = E_{Ag/AgCl} + 0.059 \times pH + 0.197$. The pH value of CO_2-saturated electrolyte was 8.06, and that of Ar-saturated electrolyte was 9.95.

2.8. Product quantification and identification

Determination of gaseous products (CO and H_2). The quantitative analysis of H_2 and CO was carried out by gas chromatography (Agilent 7890a) with a thermal conductivity detector. A thermal conductivity detector (TCD) was used to quantify H_2, and a flame ionization detector (FID) equipped with a mechanizer was used to quantify CO.

Determination of ammonia. The quantification of ammonia concentration was conducted using the improved salicylic acid spectrophotometry method (HJ536-2009). In detail, 2.0 mL of 1 M NaOH solution containing 0.2 M salicylic acid and 0.4 M sodium citrate dihydrate, 1.0 mL of 0.05 M sodium hypochlorite solution and 0.2 mL of 1% mass fraction of sodium nitroferricyanide aqueous solution were added to 2.0 mL of electrolyte obtained from the cathodic chamber, followed by thorough mixing and incubation in a dark environment for 1 h, and finally its absorbance was measured at 653 nm. The standard curve of the quantification of ammonia is shown in Fig. S8.

Determination of urea. Urea concentration was detected *via* urease decomposition. 0.2 mL of urease solution with a concentration of 5 mg mL^{-1} was added into 1.8 mL of urea electrolyte and then reacted at 37 °C in a water bath for 40 min. Urea, CO $(NH_2)_2$, was decomposed using urease into CO_2 and two NH_3 molecules. After the decomposition, the NH_3 concentration in urea electrolyte with urease was detected *via* the above ammonia quantitative method. At the same time, the NH_3 concentration in urea electrolyte without urease was also quantified. The total moles (m_{urease}) of ammonia in the electrolyte were measured using a spectrophotometer and expressed as $2m_{urea} + m_{ammonia}$, where $2m_{urea}$ represents the moles of ammonia coming from the decomposition. Therefore, the moles of urea (m_{urea}) produced were calculated as $(m_{urease} - m_{ammonia})/2$. The standard curve of the quantification of urea is shown in Fig. S9.

Determination of NO_2^-–N. The quantification of NO_2^-–N concentration was conducted using the spectrophotometry method. 0.5 g sulfanilic acid was dissolved in 90 mL of DIW and 5 mL of acetic acid. Then, 5 mg *N*-(1-naphthyl)-ethylenediamine dihydrochloride was added and the solution was increased to 100 mL to obtain a chromogenic agent. The electrolyte after testing was taken out and diluted to an appropriate concentration. 1 ml of the treated electrolyte was mixed with 4 ml of the chromogenic agent and kept in the dark for 15 minutes. The standard curve of the quantification of NO_2^-–N is shown in Fig. S11.

2.9. Calculation of faradaic efficiency and yield rate

The faradaic efficiency is the ratio of the number of electrons transferred for the formation to the total amount of electricity that flows through the circuit. The faradaic efficiency of urea production was calculated according to the charge consumed for urea synthesis and the actual charge generated during the electroreduction test:

$$FE_{urea} = \frac{z \times C_{urea} \times V_{aq} \times F}{M_{urea} \times Q} \times 100\%$$

$$\text{Yield rate}_{urea} = \frac{C_{urea} \times V_{aq}}{t \times m_{cat.}}$$

where z is the number of transferred electrons ($z = 16$), C_{urea} is the concentration of urea in ppm, V_{aq} is the volume of electrolyte in the cathode compartment, F is the faradaic constant (96 485 C mol^{-1}), M_{urea} is the molar mass of urea (M_{urea} = 60.06 g mol^{-1}), Q is the total charge amount, t (h) is the reduction time and $m_{cat.}$ (g) is the catalyst loading mass.

3. Results and discussion

3.1. Structural characterization of electrocatalysts

Primarily, a new process was developed to prepare $Cu_2(OH)_2CO_3$, which can be obtained by simply adjusting the ratio of Na_2CO_3 and $Cu(NO_3)_2$ without adjusting the pH and then by low-temperature roasting. $Cu(OH)_2$, on the other hand, is obtained by adding ammonia solution and NaOH aqueous solution successively to $Cu(NO_3)_2$ solution.[36] Evidenced by X-ray diffraction (XRD), the obtained samples were monoclinic $Cu_2(OH)_2CO_3$ and orthorhombic $Cu(OH)_2$ (PDF#76-0660 and PDF#13-0420) without any detectable impurity phases (Fig. 2b). Their Raman spectra matched perfectly with the reported standard spectra (Fig. 2c).[39,40] To determine the surface chemical status of $Cu_2(OH)_2CO_3$ and $Cu(OH)_2$, XPS was employed. The Cu 2p XPS signals can be observed at 935.5 and 954.9 eV (Fig. S1b), which confirms the valence state of Cu^{2+} in the pristine catalyst. A new peak at 289.7 eV in the C 1s spectrum of $Cu_2(OH)_2CO_3$ compared to $Cu(OH)_2$ can be attributed to CO_3^{2-} (Fig. 2d).[41] The O 1s spectrum also indicates this (Fig. S1c).[42]

In order to understand the pore structure of the catalyst, a BET (Brunauer–Emmett–Teller) test was performed. The N_2 adsorption–desorption curves indicated that both catalysts were mesoporous, whereas the pore size distribution plots showed that micropores with pore sizes of ~2.5 nm were pre-

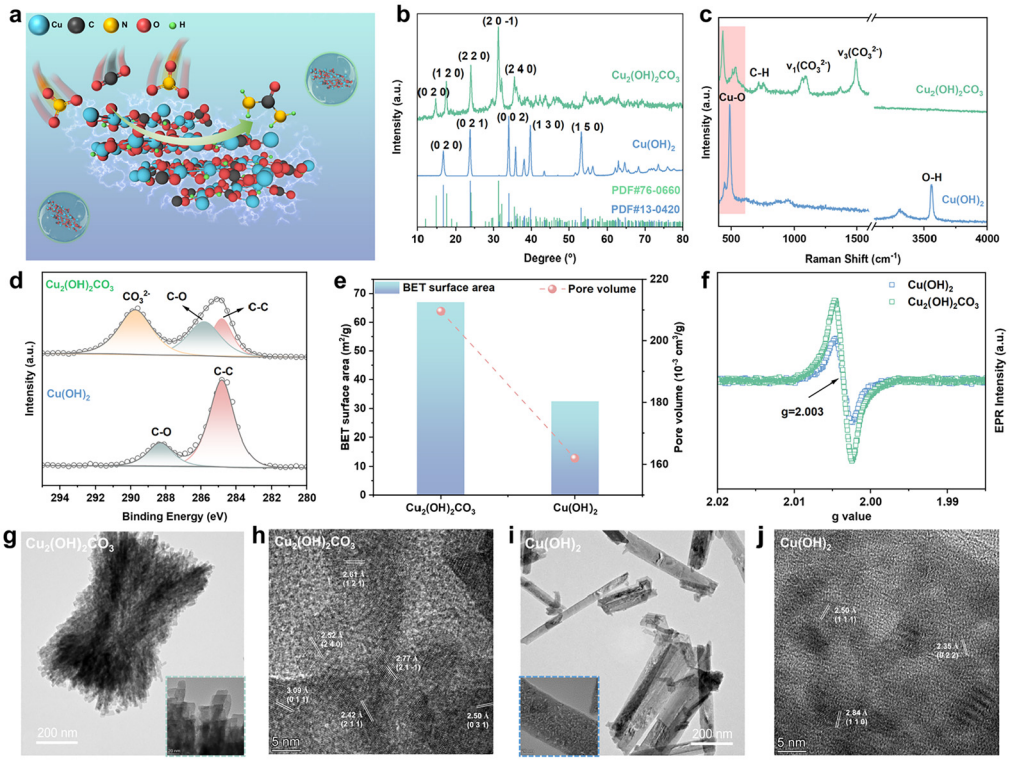

Fig. 2 Structural characterization of $Cu_2(OH)_2CO_3$ and $Cu(OH)_2$ electrocatalysts. (a) Illustration for the urea synthesis process on the surface of $Cu_2(OH)_2CO_3$. (b) XRD pattern. (c) Raman spectrum. (d) C 1s XPS spectrum. (e) BET surface area and pore volume. (f) EPR spectrum. (g) TEM images of $Cu_2(OH)_2CO_3$ at a 200 nm scale (inset: 20 nm). (h) HRTEM image of $Cu_2(OH)_2CO_3$. (i) TEM images of Cu $(OH)_2$ at a 200 nm scale (inset: 20 nm). (j) HRTEM image of Cu $(OH)_2$.

dominantly present in $Cu_2(OH)_2CO_3$ (Fig. S2). This strengthens the plausibility that the BET specific surface area and the pore volume of $Cu_2(OH)_2CO_3$ are much larger than those of Cu $(OH)_2$ (Fig. 2e). The electron paramagnetic resonance (EPR) spectrum is selected to analyze oxygen vacancies (V_o) in catalysts.[43] The EPR signal at g = 2.003, which represents unpaired electrons, confirmed the presence of V_o. The EPR spectrum indicates that V_o is more abundant in $Cu_2(OH)_2CO_3$ (Fig. 2f).[44,45]

Both the representative scanning electron microscopy (SEM) images (Fig. S4a and b) and transmission electron microscopy (TEM) images (Fig. 2g) of $Cu_2(OH)_2CO_3$ reveal that the catalyst exhibits a hierarchical flower-like architecture assembled from densely packed nanoscale primary units, giving rise to a rough and open framework. In contrast, Cu $(OH)_2$ is mainly composed of elongated rod-like crystallites and displays a more uniform one-dimensional morphology (Fig. 2i and Fig. S5a and b). The TEM images further reveal that $Cu_2(OH)_2CO_3$ consists of loosely assembled nanoscale building blocks, whereas $Cu(OH)_2$ is dominated by discrete nanorods. HRTEM images of $Cu_2(OH)_2CO_3$ show multiple lattice fringes in adjacent regions, suggesting a richer facet exposure and locally heterogeneous coordination environments. By comparison, $Cu(OH)_2$ exhibits a more regular lattice arrangement (Fig. 2h and j). These results indicate that $Cu_2(OH)_2CO_3$ possesses stronger nanoarchitectural heterogeneity than $Cu(OH)_2$, which is expected to favor a more spatially nonuniform and gradual cathodic reconstruction process. Such structural heterogeneity may help sustain a broader mixed-valence Cu working-state window during electrolysis, thereby promoting the temporal coexistence of carbon- and nitrogen-containing intermediates and increasing the probability of C–N coupling.

3.2. Electrocatalytic performance for urea synthesis

The electrocatalytic selectivity of $Cu_2(OH)_2CO_3$ and $Cu(OH)_2$ for urea synthesis in H-type cells was evaluated by the chronoamperometry (CA) method. The as-employed electrolyte (0.1 M $KHCO_3$ and 0.05 M KNO_3) was saturated with high-purity CO_2 bubbles, which flowed continuously to the cathode during CA testing. Urea production was measured using the indophenol blue colorimetric method (Fig. S9). In the first place, the mass loading was optimized based on the obtained FE, as shown in Fig. S7b. Electrocatalytic tests were performed at potentials ranging from −0.5 to −1.0 V *versus* RHE, where CA and ultraviolet-visible (UV-Vis) results are shown in Fig. S12. As shown in Fig. 3a, $Cu_2(OH)_2CO_3$ exhibits a larger double-layer capacitance (C_{dl} = 35.4 μF cm^{-2}) than $Cu(OH)_2$ (C_{dl} = 16.9 μF cm^{-2}), indicating a higher electrochemically accessible interfacial area. The total current density of $Cu_2(OH)_2CO_3$ is significantly

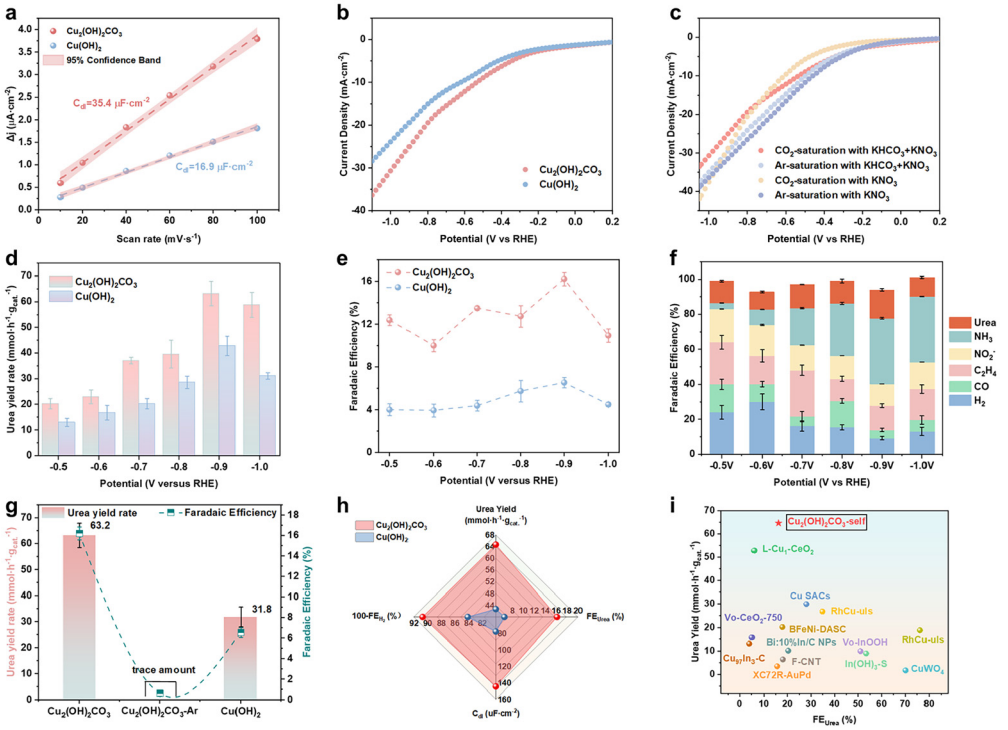

Fig. 3 Electrocatalytic performance of urea synthesis. (a) C_{dl} and (b) LSV curves of $Cu_2(OH)_2CO_3$ and $Cu(OH)_2$. (c) LSV curves of $Cu_2(OH)_2CO_3$ under different conditions. (d) Urea yield rate and (e) FEs at different potentials for $Cu_2(OH)_2CO_3$ and $Cu(OH)_2$ in 0.1 M $KHCO_3$ and 0.05 M KNO_3 electrolyte with CO_2 feeding gas. (f) The faradaic efficiencies for primary products of $Cu_2(OH)_2CO_3$ at various applied potentials. (g) Urea synthesis performance comparison between $Cu_2(OH)_2CO_3$ and $Cu(OH)_2$ at −0.9 V *versus* RHE. (h) Comparison of FE_{urea}, urea yield, C_{dl} and 100-FE_{H_2} between $Cu_2(OH)_2CO_3$ and $Cu(OH)_2$. (i) Comparison of the FEs of reported catalysts and that of $Cu_2(OH)_2CO_3$ using NO_3^- as the nitrogen source. The error bars represent the standard deviation for at least three independent measurements.

higher than that of $Cu(OH)_2$ within the test potential range, indicating that it exhibits a stronger response to the electrochemical synthesis of urea (Fig. 3b). For $Cu_2(OH)_2CO_3$, the polarization curves recorded under different gas atmospheres and electrolytes (Fig. 3c) are clearly different from each other, indicating that its cathodic response is sensitive to both the reactant environment and the electrolyte composition. In particular, the change between CO_2-saturated and Ar-saturated conditions in the same $KHCO_3$ + KNO_3 electrolyte confirms that the catalyst responds differently when CO_2 is introduced in the presence of nitrate, which is consistent with its ability to operate under CO_2/NO_3^- co-reduction conditions. The catalytic performance data further highlight the difference between the two catalysts. As shown in Fig. 3d, $Cu_2(OH)_2CO_3$ delivers a higher urea yield rate than $Cu(OH)_2$ at all applied potentials. The product yields at each potential were averaged over three independent measurements. A similar trend is observed for faradaic efficiency (Fig. 3e), where $Cu_2(OH)_2CO_3$ consistently outperforms $Cu(OH)_2$ across the whole potential range. For both catalysts, the urea yield rate and FE first increase with increasing cathodic bias and then decline at more negative potentials, indicating the existence of an optimal potential window for urea formation. Besides urea, a series of side products were quantified by spectrophotometric and gas chromatographic analysis, including ammonia (NH_3), nitrite (NO_2^-), carbon monoxide (CO), ethene (C_2H_4), and hydrogen (H_2) (Fig. S8–11). By comparing the side products at each potential under $Cu_2(OH)_2CO_3$ catalysis, it was found that the gaseous product H_2 was produced in the least amount and NH_3 in the most amount at −0.9 V *versus* RHE, implying that the achievement of high urea yield and selectivity requires the reduction of competitive hydrogenation reactions and the conversion of as much NO_3^- to NH_3 as possible (Fig. 3f).

This can also be seen by comparing the urea yield and selectivity of $Cu_2(OH)_2CO_3$ and $Cu(OH)_2$ at −0.9 V *versus* RHE (Fig. 3f and g). The highest urea yield rate of 63.20 mmol h^{-1} $g_{cat.}^{-1}$ and a high FE of 16.21% for $Cu_2(OH)_2CO_3$ were achieved at −0.9 V *versus* RHE, superior to those of noble-metal based electrocatalysts. At the same applied potential, $Cu_2(OH)_2CO_3$ eclipses the catalytic urea production yield of $Cu(OH)_2$ by a factor of 2. The control experiment also shows that a significant amount of urea product is formed only when CO_2 gas is passed into the electrolyte, suggesting that urea does indeed originate from the co-electrolysis of NO_3^- and CO_2 rather than $KHCO_3$. However, the product distribution shows that a considerable fraction of electrons is still consumed by competing reactions, including the HER, nitrate reduction to NH_3, and CO_2 reduction to carbon-containing by-products. The decrease in urea FE at more negative potentials further suggests that excessive polarization accelerates these competing pathways,

particularly the HER and over-reduction of nitrogen-containing intermediates. Furthermore, the performance parameters of the two copper-derived catalysts in electrosynthesis of urea were comprehensively compared, and $Cu_2(OH)_2CO_3$ was superior to $Cu(OH)_2$ in terms of FE_{urea}, urea yield, C_{dl} (Fig. S6) and 100-FE_{H_2} (Fig. 3h and Fig. S13). It can be attributed to the fact that $Cu_2(OH)_2CO_3$ is better able to form and maintain a mixed-valence Cu^+/Cu^0 state during electrocatalysis, where the presence of Cu^+ facilitates the stabilization of intermediates, thereby promoting C–N bond coupling. Notably, $Cu_2(OH)_2CO_3$ exhibits a competitive urea yield rate among reported electrocatalytic urea synthesis systems using CO_2 and NO_3^- as carbon and nitrogen sources, although its faradaic efficiency is not the highest among the reported catalysts (Fig. 3i).[11–15,17,18,21,46–58] The present comparison therefore highlights not only the catalytic activity of $Cu_2(OH)_2CO_3$, but more importantly the role of precursor-regulated reconstruction in improving C–N coupling relative to $Cu(OH)_2$ under identical reaction conditions. Compared with $Cu(OH)_2$, $Cu_2(OH)_2CO_3$ maintains a broader Cu^{2+}–Cu^+–Cu^0 mixed-valence working-state window during electrolysis (Fig. 4 and SI Fig. S16–S18). This reconstructed mixed-valence interface favors the temporal coexistence of carbon- and nitrogen-containing intermediates and thus promotes their subsequent C–N coupling. Admittedly, the selectivity of $Cu_2(OH)_2CO_3$-catalyzed urea electrosynthesis still has plenty of headroom for improvement. Due to the restructuring that occurs during the electrochemical reduction process, the long-term performance of $Cu_2(OH)_2CO_3$ is far from ideal. This is also a major challenge that we need to overcome in our future research.

3.3. Evidence of Cu^+–Cu^0 during the urea electrosynthesis

It has been demonstrated that Cu-based catalysts undergo inevitable and uncontrollable reconstruction and produce mixed oxidation states of Cu (*e.g.*, Cu^{2+}, Cu^+, and Cu^0) during the electroreduction process. Changes in the valence state of Cu species play a key role in the conversion of CO_2 to C_{2+} products.[59,60] To understand the specific morphology of Cu species in $Cu_2(OH)_2CO_3$ during electrocatalytic urea synthesis, an in-depth study was carried out. X-ray photoelectron spectroscopy and X-ray absorption spectroscopy spectra reveal the Cu oxidation states in both $Cu_2(OH)_2CO_3$ and $Cu(OH)_2$. The valence states of the Cu species were all +2 before the reaction (Fig. S15). After electrolysis, the X-ray absorption near-edge structure (XANES) edge of $Cu_2(OH)_2CO_3$ shifts markedly to lower energy relative to the fresh sample, confirming substantial reduction of Cu species under working conditions. However, the Cu K-edge position remains between those of Cu foil and Cu_2O references, implying the coexistence of metallic Cu (Cu^0) and Cu(I) oxide (Cu^+) phases (Fig. 4a–c). Consistently, the Fourier-transformed EXAFS spectra and wavelet-transform analysis show that the fresh sample is dominated by Cu–O coordination, whereas the electrolyzed sample exhibits a strong Cu–Cu contribution, demonstrating pronounced struc-

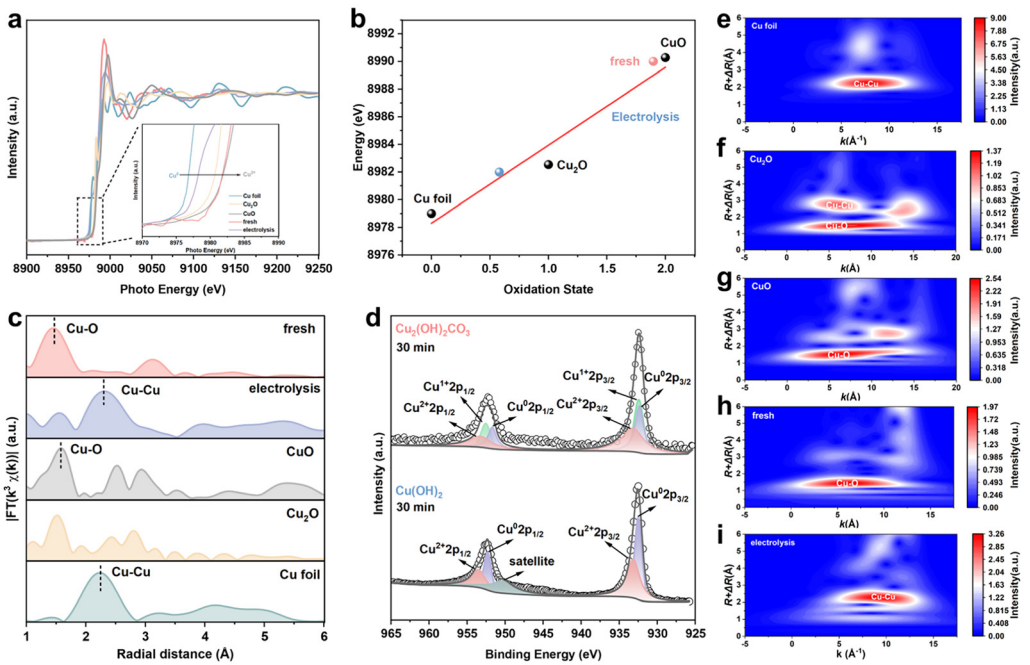

Fig. 4 Catalyst surface valence changes during electrosynthesis of urea. (a) Normalized Cu K-edge XANES spectra and (b) corresponding oxidation state fitting for different copper species. (c) Cu K-edge FT-EXAFS spectra without phase correction. (d) High-resolution Cu 2p spectrum of loaded $Cu_2(OH)_2CO_3$ and $Cu(OH)_2$ electrodes. Wavelet transforms of the k^3-weighted Cu K-edge EXAFS signals for (e) Cu foil, (f) Cu_2O, (g) CuO, and $Cu_2(OH)_2CO_3$ electrodes with the reaction of (h) 0 min and (i) 30 min. After the electrodes reacted for 30 min at −0.9 V *versus* RHE, they were immediately transferred to an air-insulated glove box, rinsed with deionized water and protected with Ar. The samples were then characterized by quasi-*in situ* X-ray absorption spectroscopy and XPS testing.

tural reconstruction during the reaction (Fig. 4e–i). These results indicate that $Cu_2(OH)_2CO_3$ follows a more gradual and broader precursor-regulated reconstruction pathway than $Cu(OH)_2$, allowing multiple Cu valence states to coexist over a longer reaction period rather than rapidly converging to a Cu^0-dominated surface.

On the other hand, quasi-*in situ* XPS further reveals that $Cu_2(OH)_2CO_3$ and $Cu(OH)_2$ exhibit clearly different reduction behaviors during electrocatalytic C–N coupling. For $Cu_2(OH)_2CO_3$, the Cu 2p spectra collected after 15 min of electrolysis at −0.9 V *versus* RHE already show a pronounced Cu^+ contribution together with residual Cu^{2+} species (Fig. S16a and b), while the spectra acquired after 30 min can still be deconvoluted into Cu^{2+}, Cu^+, and Cu^0 components. Further proceeding to 30 min, Cu^+ is converted into Cu^0, at which point three valence states of Cu species coexist on the electrode surface (Cu^{2+}, Cu^+ and Cu^0) (Fig. 4d). This assignment is further supported by the quasi-*in situ* Cu LMM spectrum at 30 min, in which Cu, Cu_2O, and CuO signals can all be identified (Fig. S16c). In contrast, $Cu(OH)_2$ follows a different evolution pathway. Its Cu 2p spectra are mainly characterized by Cu^{2+} and Cu^0 features, and the corresponding Cu LMM spectrum at 30 min is dominated by the metallic Cu component with only a minor oxidized contribution (Fig. 4e and Fig. S17).

Therefore, $Cu_2(OH)_2CO_3$ has a better ability to maintain the mixed oxidation state of Cu during electrocatalytic reduction compared to $Cu(OH)_2$, especially the longer presence of Cu^+. This can also be demonstrated by the redox behavior of both catalysts in 0.1 M KOH aqueous solution (Fig. S18a and b). Two reduction peaks were observed in the CV curve of $Cu_2(OH)_2CO_3$ at 1.08 and 0.16 V *versus* RHE, corresponding to the reduction of Cu^{2+} to Cu^+ and then to Cu^0, respectively. In contrast, for $Cu(OH)_2$ only one reduction peak is observed at 0.18 V, which can be attributed to the direct reduction of Cu^{2+} to Cu^0. This further suggests that $Cu(OH)_2$ could not maintain the presence of Cu^+ well. The LSV curve in Fig. S18c also supports this idea. These results indicate that $Cu_2(OH)_2CO_3$ follows a more gradual and broader precursor-regulated reconstruction pathway than $Cu(OH)_2$, allowing multiple Cu valence states to coexist over a longer reaction period rather than rapidly converging to a Cu^0-dominated surface. When combined with the surface-sensitive XANES and XPS results, these synchrotron data suggest that electrolysis drives $Cu_2(OH)_2CO_3$ toward a partially reduced working state in which Cu–Cu coordination is formed while oxidized Cu species are still retained at the interface. Such a broadened mixed-valence working-state window is consistent with a more heterogeneous catalytic interface and provides a reasonable structural basis for the improved C–N coupling performance of $Cu_2(OH)_2CO_3$ relative to $Cu(OH)_2$.

3.4. *In situ* tracking of the surface species

The *in situ* SR-FTIR measurements were carried out on $Cu_2(OH)_2CO_3$ to monitor the evolution of the bonding structure of electrochemically generated intermediate species. The infrared signals are collected from 1000 to 4000 cm^{-1} during a negative scan from −0.5 to −1.0 V *versus* RHE (Fig. 5a). For the range from 1700 to 2200 cm^{-1} (Fig. 5b), infrared bands at ~1990 cm^{-1} corresponding to the stretching mode of N═O were observed, associated with the co-activation of nitrate ions on the catalyst.[61] In the working state (potential range from −0.7 to −1.0 V *vs.* RHE), the peak at 1866 cm^{-1} is assigned to the *NHCO species.[62] It should be noted that the vibration of *NHCO intensity increases with increasing applied negative potential and reaches the maximum value at around −1.0 V, which is in good accordance with the electrochemical test results, implying that the formation of intermediate species, especially *NHCO, is closely related to the urea generation. Meanwhile, the C–N vibration bond observed at 1360 cm^{-1} is strong evidence that coupling of CO_2 and NO_3^- reduction occurs (Fig. 5c).[13] Infrared bands probed at 1213 and 1486 cm^{-1} are assignable to the wagging mode of $–NH_2$ in urea and OCO vibrational bands.[63,64] These results explicitly justify the presence of the $*CONH_2$ intermediate.

3.5. DFT calculations of C–N coupling mechanism

To further unravel the fundamental origins of the high selectivity of $Cu_2(OH)_2CO_3$, density functional theory (DFT) calculations were conducted on the preferentially oriented (0 1 0) (equivalent to the (0 2 0) crystal plane) direction of the $Cu_2(OH)_2CO_3$ crystal (Fig. S20) corresponding to the XRD and TEM results. We first investigated the activation capacity of $Cu_2(OH)_2CO_3$ and $Cu(OH)_2$ catalysts toward nitrate and CO_2. The adsorption of NO_3^- and CO_2 by both catalysts is a process of decreasing free energy (Fig. S21). For NO_3^-, it can be immobilized on the surface of $Cu_2(OH)_2CO_3$ through a bidentate binuclear coordination mode with an adsorption energy of −2.19 eV ($Cu(OH)_2$ exhibits a bidentate mononuclear coordination mode with an adsorption energy of −2.00 eV) (Fig. S22 and S24). In contrast, CO_2 was only adsorbed on the catalyst surface by physical adsorption (Fig. S25).[65]

The quasi-*in situ* XANES and XPS results indicate that $Cu_2(OH)_2CO_3$ undergoes reconstruction to produce Cu^0 and Cu^+ during the reaction (Fig. 4 and Fig. S16–18). The (010) facet is rich in hydroxyl, and thus we adjusted the number of surface hydroxyls to ensure the reasonable valence state of Cu. Fig. 6 shows the detailed free-energy diagram of the corresponding structures with the lowest energy pathway from CO_2 and NO_3^- to urea on the Cu^+–Cu^0 sites. The urea production initiates from the thermodynamically spontaneous reduction of NO_3^- to the $*NO_2$ intermediate on the Cu^0 site with an adsorption free energy of −3.56 eV. Correspondingly, CO_2 is spontaneously adsorbed on the surface of the Cu^+ site with a free energy of −0.42 eV. The hydrogenation of $* CO_2$ is the first free energy rise step with a 0.45 eV uphill in reaction-free energy; thereafter, the *COOH was spontaneously reduced to *CO thermodynamically. In the following reaction path, from step 4 to step 10, *CO is stably located at the Cu^+ site on the surface of $Cu_2(OH)_2CO_3$. However, $*NO_2$ undergoes the reduction of $*NO_2 \rightarrow *NOOH \rightarrow *NO \rightarrow *NHO \rightarrow *NHOH \rightarrow *NH \rightarrow *NH_2$ in this process. This indicates that the Cu^+ site has strong stability towards *CO. As $*NH_2$ was formed, the *CO

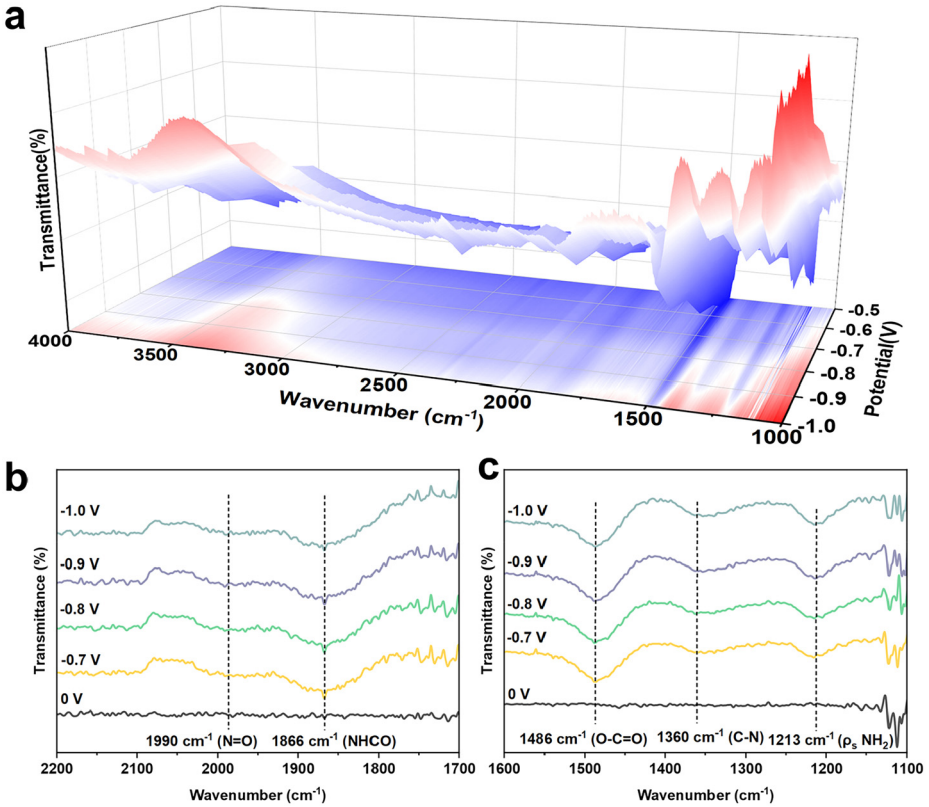

Fig. 5 *In situ* FTIR spectroscopy measurements under various potentials for $Cu_2(OH)_2CO_3$ during electrocatalytic coupling of NO_3^- and CO_2. (a) Three-dimensional FTIR spectra in the range of 1000–4000 cm^{-1}. (b) Infrared signals in the range of 1700–2200 cm^{-1}. (c) Infrared signals in the range of 1100–1600 cm^{-1}.

intermediate was involved in the urea production. C–N coupling is a decisive step in the overall reaction. In contrast with the reaction-free energy for hydrogenation of $*NH_2$ to $*NH_3$ (0.91 eV), the lower reaction-free energy of 0.59 eV for the formation of the key intermediate $*NH_2CO$ (inset in Fig. 6a) on the Cu^+–Cu^0 sites was beneficial for the direct C–N coupling at step 11. Subsequently, $*NH_2CO$ and $*NO_2$ rapidly bound together and spontaneously converted into $*NO_2NH_2CO$ with a free energy of −3.21 eV. Subsequently $*CONO_2NH_2$ is further protonated to $*CO(NH_2)_2$ with a free energy of −1.78 eV, which is desorbed from the catalyst surface to the electrolyte to form urea. Furthermore, the lower reaction-free energy of C–N coupling between the *CO and $*NH_2$ intermediates and the thermodynamically spontaneous formation pathway determine the extremely high selectivity of urea electrosynthesis on the Cu^+–Cu^0 sites, in line with the preceding experimental analysis.

3.6. Urea electrosynthesis in food-waste biological treatment

To validate the feasibility of $Cu_2(OH)_2CO_3$ electrocatalytic C–N coupling for urea synthesis in real environmental scenarios, we performed electrocatalytic experiments using CO_2 and NO_3^- generated during food-waste biological treatment (Fig. 7a). Considering the effects of low CO_2 partial pressure, dilute NO_3^- concentration and co-existing high NH_4^+ levels on electrochemical urea formation in practice, we explored the performance of urea electrosynthesis in simulated and actual scenarios. The LSV curves showed that, at the same applied potential, the current density was higher under pure CO_2 saturation (Fig. 7b). Saturation with 30% CO_2 and 70% CH_4 led to a marked decrease in current density, attributable to reduced CO_2 mass transfer and lower dissolved CO_2 concentration (CH_4 hardly participated in the electrochemical reduction), which limits the C–N coupling reaction. Instead, using the actual anaerobic digestion effluent as the electrolyte produced an increase in current density, likely owing to the participation of coexisting salts and soluble proteins in the real effluent. We demonstrate that using actual food-waste anaerobic effluent together with the CO_2 and CH_4 gas produced by aerobic composting enables electro-catalyzed C–N coupling to generate urea with a yield rate of 11.1 mmol h^{-1} $g_{cat.}^{-1}$ and a FE of 1.96% at −0.9 V *versus* RHE (Fig. 7c). The NO_3^-–N concentration in the real effluent is 269.54 ± 2.71 mg L^{-1}, lower than that in the optimized 0.05 M KNO_3 electrolyte, which restricts the generation of nitrogen-containing intermediates and causes a significant decrease in urea yield and selectivity (Fig. 7c and d and SI Fig. S25). Furthermore, the real effluent contains high concentrations of NH_4^+–N, soluble proteins, phosphate, suspended/volatile solids, and oxidizable organic species. These coexisting components may compete for adsorption on the reconstructed Cu surface, partially block

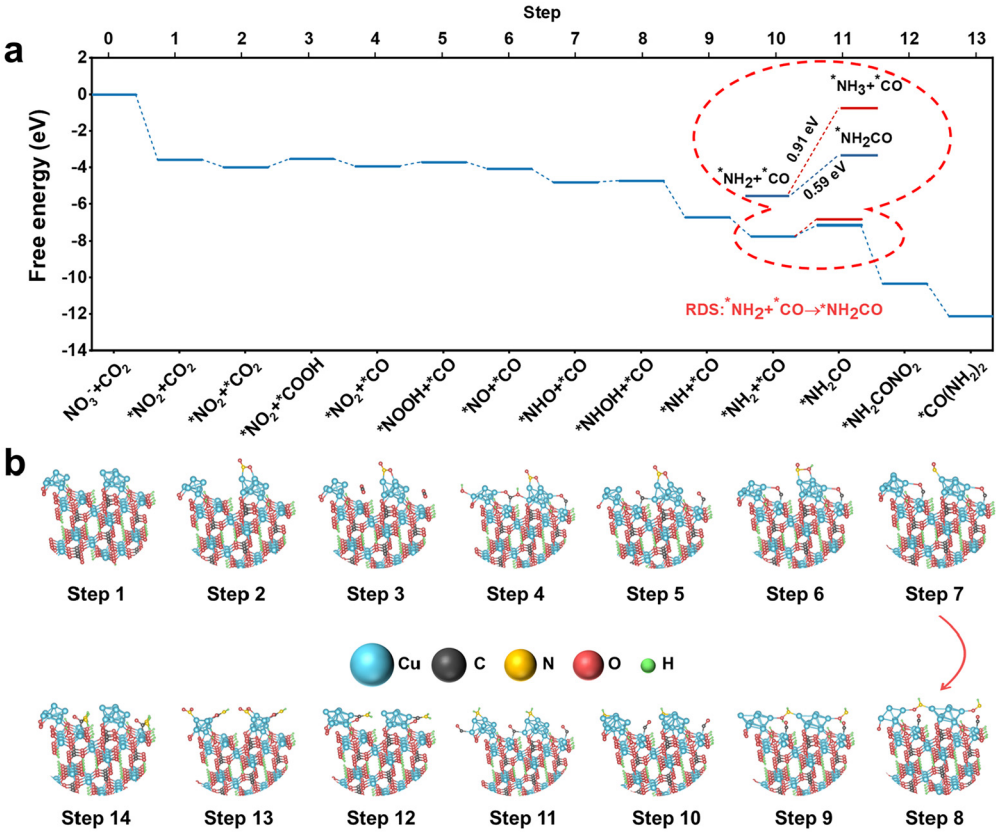

Fig. 6 DFT calculations for urea synthesis. (a) Free-energy diagram for urea production at the Cu^{+}–Cu^{0} sites on the (010) facets of $Cu_2(OH)_2CO_3$. (b) Corresponding atomic configurations for each step.

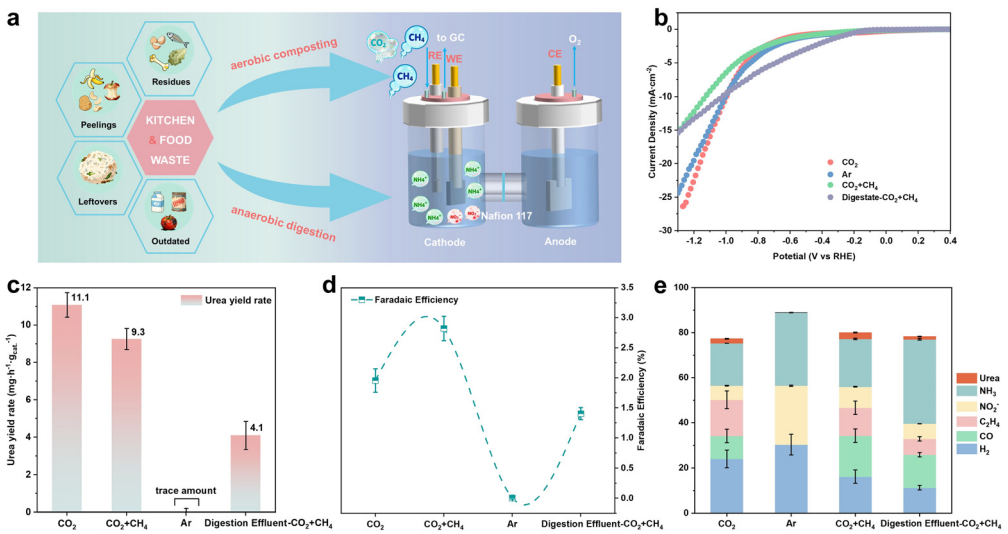

Fig. 7 Urea electrosynthesis from food-waste biological treatment. (a) Diagram of urea electrosynthesis using CO_2 and NO_3^- generated during food-waste biological treatment. (b) LSV curves. (c) Yield rate. (d) FEs and (e) major product distributions for urea electrosynthesis from simulated and actual food-waste anaerobic digestion effluents under different atmospheres at −0.9 V *versus* RHE. The simulated digestion effluent consisted of 0.2 M NH_4HCO_3 and 0.01 M KNO_3; the aerobic-composting gas composition was 30% CO_2 and 70% CH_4.

active sites, and introduce parasitic electrochemical reactions. Consistently, electrochemical measurements show that the real digestion effluent decreases the electrochemically active surface area and increases the solution/internal resistance and electrode resistance (Fig. S28). It is noteworthy that, when the atmosphere was changed from pure CO_2 to 30% CO_2 and 70%

CH_4, the urea yield decreased while selectivity increased. This can be explained by CH_4 suppressing the individual CO_2RR, which is consistent with the observed decrease in C_2H_4 selectivity in the product distribution (Fig. 7e).

4. Conclusion

The electrocatalytic coupling of CO_2 with NO_3^- for direct urea synthesis shows gigantic potential as an alternative to the traditional process. We have demonstrated that precursor chemistry plays a decisive role in regulating the reconstruction pathway of Cu-based catalysts during electrocatalytic urea synthesis from CO_2 and nitrate. By systematically comparing $Cu_2(OH)_2CO_3$ and $Cu(OH)_2$, we show that the hierarchically structured $Cu_2(OH)_2CO_3$ delivers a urea yield of 63.20 mmol h^{-1} $g_{cat.}^{-1}$ with a faradaic efficiency of 16.21% at −0.9 V *versus* RHE, establishing a highly productive pathway for scalable green synthesis. Quasi-*in situ* XPS and XANES results reveal that $Cu_2(OH)_2CO_3$ undergoes a more gradual and broader reconstruction process, during which a mixed-valence Cu working-state window composed of Cu^{2+}, Cu^+, and Cu^0 can be maintained over the course of electrolysis. In contrast, $Cu(OH)_2$ tends to evolve more directly toward a Cu^0-dominated surface. This distinct precursor-regulated reconstruction pathway provides a reasonable structural basis for the superior C–N coupling performance of $Cu_2(OH)_2CO_3$. Furthermore, *in situ* FTIR and theoretical calculations showed that electrochemical CO_2 reduction and NO_3^- reduction first proceed independently until *CO and *NH_2 are formed. The persistence of Cu^+ together with Cu^0 under operating conditions is expected to increase the temporal coexistence of carbon- and nitrogen-containing reactive species at the catalyst interface, thereby favoring urea formation. Combined with the hierarchical nanoarchitecture of $Cu_2(OH)_2CO_3$, such a broadened mixed-valence working state is closely associated with its enhanced catalytic activity and selectivity. Crucially, the exceptional matrix tolerance exhibited by $Cu_2(OH)_2CO_3$ in real food waste leachate highlights the practical viability of this system. We also proved the feasibility of direct electrocatalytic C–N coupling for urea production using CO_2 and NO_3^- from food waste biological treatment. Different from these previously reported strategies based mainly on static interface construction, defect engineering, or molecular coordination regulation, the present work emphasizes the role of precursor-regulated reconstruction in determining the working-state structure of Cu-based catalysts. The carbonate/hydroxide-rich $Cu_2(OH)_2CO_3$ precursor undergoes a more gradual cathodic reconstruction than $Cu(OH)_2$ and maintains a broader Cu^{2+}–Cu^+–Cu^0 mixed-valence window during electrolysis. This dynamic mixed-valence interface favors the coexistence of *CO and nitrogen-containing intermediates and thus promotes subsequent C–N coupling. This provides a broader perspective for the efficient utilization of the key hydroxylamine-carbonyl C–N coupling reaction for the electrochemical synthesis of other more complex organic nitrogen compounds from inexpensive inorganic feedstocks.

Author contributions

Ke Wu conceived the work, performed the experiments independently, analyzed and processed the data, and wrote the paper. Guojie Ye contributed to XPS data processing and analysis. Zhengwei Zhou conducted formal analysis and data curation. All authors participated in the discussion and analysis of the paper. Zuofeng Chen and Zhendong Lei contributed to writing – review & editing and conceptualization. Deli Wu contributed to writing – review & editing, supervision, funding acquisition, and conceptualization.

Conflicts of interest

The authors declare that they have no known competing financial interests or personal relationships that could have appeared to influence the work reported in this paper.

Data availability

The data supporting the findings of this study are included within the main article and the supplementary information (SI). Materials; DFT computational details; FTIR and supplementary XPS, BET spectrums, and SEM images of the materials (Fig. S1–S5); optimization of material electrochemical properties and C-N coupling parameters (Fig. S6–S7; Fig. S12–S14); quantitative analysis of products (Fig. S8–S11); SEM images and XPS spectra of the catalyst material before, after, and during the reaction (Fig. S15–S19); calculation of adsorption and reaction free energies (Fig. S20–S25); electrochemical testing of urea electrosynthesis in real environmental scenarios (Table S1; Fig. S26–S28). Supplementary information is available. See DOI: https://doi.org/10.1039/d6gc02101h.

Acknowledgements

This work was financially supported by the National Key R&D Program of China (2023YFC3905600) and the National Natural Science Foundation of China (NSFC, No: 52170091 and 42377390). The authors gratefully acknowledge the BL11B, BL14W1, BL08U1A, and BL13SSW stations at the Shanghai Synchrotron Radiation Facility.

References

1 X. Fu, J. B. Pedersen, Y. Zhou, M. Saccoccio, S. Li, R. Sažinas, K. Li, S. Z. Andersen, A. Xu, N. H. Deissler, J. B. V. Mygind, C. Wei, J. Kibsgaard, P. C. K. Vesborg, J. K. Nørskov and I. Chorkendorff, *Science*, 2023, **379**, 707–712.

2 Z. Liu, D. Guan, W. Wei, S. J. Davis, P. Ciais, J. Bai, S. Peng, Q. Zhang, K. Hubacek, G. Marland, R. J. Andres, D. Crawford-Brown, J. Lin, H. Zhao, C. Hong, T. A. Boden,

K. Feng, G. P. Peters, F. Xi, J. Liu, Y. Li, Y. Zhao, N. Zeng and K. He, *Nature*, 2015, **524**, 335–338.
3 Y. Wu, X. Liu, Y. Huang, N. Meng and B. Zhang, *Nat. Protoc.*, 2026, DOI: 10.1038/s41596-025-01298-7.
4 H. Xu, Y. Ma, J. Chen, W.-x. Zhang and J. Yang, *Chem. Soc. Rev.*, 2022, **51**, 2710–2758.
5 B. Chang, H. Pang, F. Raziq, S. Wang, K.-W. Huang, J. Ye and H. Zhang, *Energy Environ. Sci.*, 2023, **16**, 4714–4758.
6 J. G. Chen, R. M. Crooks, L. C. Seefeldt, K. L. Bren, R. M. Bullock, M. Y. Darensbourg, P. L. Holland, B. Hoffman, M. J. Janik, A. K. Jones, M. G. Kanatzidis, P. King, K. M. Lancaster, S. V. Lymar, P. Pfromm, W. F. Schneider and R. R. Schrock, *Science*, 2018, **360**, eaar6611.
7 M. A. Mohajer, P. Basuri, A. Evdokimov, G. David, D. Zindel, E. Miliordos and R. Signorell, *Science*, 2025, **388**, 1426–1430.
8 C. Smith, A. K. Hill and L. Torrente-Murciano, *Energy Environ. Sci.*, 2020, **13**, 331–344.
9 J. Liang, Z. Li, L. Zhang, X. He, Y. Luo, D. Zheng, Y. Wang, T. Li, H. Yan, B. Ying, S. Sun, Q. Liu, M. S. Hamdy, B. Tang and X. Sun, *Chem*, 2023, **9**, 1768–1827.
10 X. Wei, Y. Liu, X. Zhu, S. Bo, L. Xiao, C. Chen, T. T. T. Nga, Y. He, M. Qiu, C. Xie, D. Wang, Q. Liu, F. Dong, C. L. Dong, X. Z. Fu and S. Wang, *Adv. Mater.*, 2023, **35**, 2300020.
11 J. Leverett, T. Tran-Phu, J. A. Yuwono, P. Kumar, C. Kim, Q. Zhai, C. Han, J. Qu, J. Cairney, A. N. Simonov, R. K. Hocking, L. Dai, R. Daiyan and R. Amal, *Adv. Energy Mater.*, 2022, **12**, 2201500.
12 X. Wei, X. Wen, Y. Liu, C. Chen, C. Xie, D. Wang, M. Qiu, N. He, P. Zhou, W. Chen, J. Cheng, H. Lin, J. Jia, X.-Z. Fu and S. Wang, *J. Am. Chem. Soc.*, 2022, **144**, 11530–11535.
13 C. Lv, C. Lee, L. Zhong, H. Liu, J. Liu, L. Yang, C. Yan, W. Yu, H. H. Hng, Z. Qi, L. Song, S. Li, K. P. Loh, Q. Yan and G. Yu, *ACS Nano*, 2022, **16**, 8213–8222.
14 X. Wu, Y. Chen, B. Tang, Q. Yan, D. Wu, H. Zhou, H. Wang, H. Zhang, D. He, H. Li, J. Zeng, L. Lu, S. Yang and T. Ma, *Nat. Commun.*, 2025, **16**, 8785.
15 Y. Yin, Z. Ling, S. Liu, Y. Wang, W. Zhao, H. Wang, J. Yang, R. Feng, S. Zhang, X. Xing, L. Jing, Q. Zhu, X. Sun, J. Zhang, X. Kang and B. Han, *Nat. Sustainability*, 2026, **9**, 108–116.
16 S. Zhang, J. Geng, Z. Zhao, M. Jin, W. Li, Y. Ye, K. Li, G. Wang, Y. Zhang, H. Yin, H. Zhang and H. Zhao, *EES Catal.*, 2023, **1**, 45–53.
17 J. Du, Y. Wu, S. Fang, D. Xu, M. Liu, H. Liang, Z. Wu, G. M. Lu and X. Wu, *Nat. Commun.*, 2025, **17**, 1008.
18 X. Liu, P. V. Kumar, Q. Chen, L. Zhao, F. Ye, X. Ma, D. Liu, X. Chen, L. Dai and C. Hu, *Appl. Catal., B*, 2022, **316**, 121618.
19 R. Tyburski, T. Liu, S. D. Glover and L. Hammarström, *J. Am. Chem. Soc.*, 2021, **143**, 560–576.
20 Y. Wu, Z. Jiang, Z. Lin, Y. Liang and H. Wang, *Nat. Sustainability*, 2021, **4**, 725–730.
21 W. Ye, Y. Zhang, L. Chen, F. Wu, Y. Yao, W. Wang, G. Zhu, G. Jia, Z. Bai, S. Dou, P. Gao, N. Wang and G. Wang, *Angew. Chem., Int. Ed.*, 2024, **63**, e202410105.
22 N. Meng, Y. Huang, Y. Liu, Y. Yu and B. Zhang, *Cell Rep. Phys. Sci.*, 2021, **2**, 100378.
23 M. Yuan, J. Chen, Y. Bai, Z. Liu, J. Zhang, T. Zhao, Q. Wang, S. Li, H. He and G. Zhang, *Angew. Chem., Int. Ed.*, 2021, **60**, 10910–10918.
24 W. Chen, H. Su, X. Chen, X. Zheng, J. Tang, Y. Li, Q. Wang and Y. Ling, *ACS Sustainable Chem. Eng.*, 2025, **13**, 18367–18376.
25 H. Ahn, R. A. Senthil, S. Jung, A. Kumar, M. Ubaidullah and M. Y. Choi, *eScience*, 2025, **5**, 100408.
26 J. Yu, J. Wang, Y. Ma, J. Zhou, Y. Wang, P. Lu, J. Yin, R. Ye, Z. Zhu and Z. Fan, *Adv. Funct. Mater.*, 2021, **31**, 2102151.
27 D. Raciti and C. Wang, *ACS Energy Lett.*, 2018, **3**, 1545–1556.
28 Y. Pang, J. Li, Z. Wang, C.-S. Tan, P.-L. Hsieh, T.-T. Zhuang, Z.-Q. Liang, C. Zou, X. Wang, P. De Luna, J. P. Edwards, Y. Xu, F. Li, C.-T. Dinh, M. Zhong, Y. Lou, D. Wu, L.-J. Chen, E. H. Sargent and D. Sinton, *Nat. Catal.*, 2019, **2**, 251–258.
29 Y. Yang, S. Louisia, S. Yu, J. Jin, I. Roh, C. Chen, M. V. Fonseca Guzman, J. Feijóo, P.-C. Chen, H. Wang, C. J. Pollock, X. Huang, Y.-T. Shao, C. Wang, D. A. Muller, H. D. Abruña and P. Yang, *Nature*, 2023, **614**, 262–269.
30 L. Zhang, J. Feng, S. Liu, X. Tan, L. Wu, S. Jia, L. Xu, X. Ma, X. Song, J. Ma, X. Sun and B. Han, *Adv. Mater.*, 2023, **35**, 2209590.
31 H. Yin, Y. Peng and J. Li, *Environ. Sci. Technol.*, 2023, **57**, 3134–3144.
32 Y. Fu, S. Wang, Y. Wang, P. Wei, J. Shao, T. Liu, G. Wang and X. Bao, *Angew. Chem., Int. Ed.*, 2023, **62**, e202303327.
33 H. Meng, Y. Yang, T. Shen, Z. Yin, L. Wang, W. Liu, P. Yin, Z. Ren, L. Zheng, J. Zhang, F.-S. Xiao and M. Wei, *Nat. Commun.*, 2023, **14**, 7980.
34 Q. Wu, R. Du, P. Wang, G. I. N. Waterhouse, J. Li, Y. Qiu, K. Yan, Y. Zhao, W.-W. Zhao, H.-J. Tsai, M.-C. Chen, S.-F. Hung, X. Wang and G. Chen, *ACS Nano*, 2023, **17**, 12884–12894.
35 S. Jiang, L. D'Amario and H. Dau, *ChemSusChem*, 2022, **15**, e202102506.
36 Q. Lei, L. Huang, J. Yin, B. Davaasuren, Y. Yuan, X. Dong, Z.-P. Wu, X. Wang, K. X. Yao, X. Lu and Y. Han, *Nat. Commun.*, 2022, **13**, 4857.
37 Y. Lum and J. W. Ager, *Angew. Chem., Int. Ed.*, 2018, **57**, 551–554.
38 Y. Yang, J. Feijóo, M. Figueras-Valls, C. Chen, C. Shi, M. V. Fonseca Guzman, Y. Murhabazi Maombi, S. Liu, P. Jain, V. Briega-Martos, Z. Peng, Y. Shan, G. Lee, M. Rebarchik, L. Xu, C. J. Pollock, J. Jin, N. E. Soland, C. Wang, M. B. Salmeron, Z. Chen, Y. Han, M. Mavrikakis and P. Yang, *Nat. Catal.*, 2025, **8**, 579–594.
39 G. Marucci, A. Beeby, A. W. Parker and C. E. Nicholson, *Anal. Methods*, 2018, **10**, 1219–1236.
40 Y. Deng, A. D. Handoko, Y. Du, S. Xi and B. S. Yeo, *ACS Catal.*, 2016, **6**, 2473–2481.
41 X. Chen, X. Wang and D. Fang, *Fullerenes, Nanotubes Carbon Nanostruct.*, 2020, **28**, 1048–1058.

42 M. Wu, X. Jiang, Y. Meng, Y. Niu, Z. Yuan, W. Xiao, X. Li, X. Ruan, X. Yan and G. He, *Chem. Eng. J. Adv.*, 2021, **8**, 100179.
43 Q. Miao, C. Nitsche, H. Orton, M. Overhand, G. Otting and M. Ubbink, *Chem. Rev.*, 2022, **122**, 9571–9642.
44 K. Zhu, F. Shi, X. Zhu and W. Yang, *Nano Energy*, 2020, **73**, 104761.
45 Y. Tao, J. Guan, J. Zhang, S. Hu, R. Ma, H. Zheng, J. Gong, Z. Zhuang, S. Liu, H. Ou, D. Wang and Y. Xiong, *Angew. Chem., Int. Ed.*, 2024, **63**, e202400625.
46 C. Chen, S. Li, X. Zhu, S. Bo, K. Cheng, N. He, M. Qiu, C. Xie, D. Song, Y. Liu, W. Chen, Y. Li, Q. Liu, C. Li and S. Wang, *Carbon Energy*, 2023, **5**.
47 S. Liu, S. Yin, Z. Wang, Y. Xu, X. Li, L. Wang and H. Wang, *Cell Rep. Phys. Sci.*, 2022, **3**, 100869.
48 Y. Liu, X. Tu, X. Wei, D. Wang, X. Zhang, W. Chen, C. Chen and S. Wang, *Angew. Chem., Int. Ed.*, 2023, **62**, e202300387.
49 X. Wei, Y. Liu, X. Zhu, S. Bo, L. Xiao, C. Chen, T. T. T. Nga, Y. He, M. Qiu, C. Xie, D. Wang, Q. Liu, F. Dong, C.-L. Dong, X.-Z. Fu and S. Wang, *Adv. Mater.*, 2023, **35**, 2300020.
50 Y. Zhao, Y. Ding, W. Li, C. Liu, Y. Li, Z. Zhao, Y. Shan, F. Li, L. Sun and F. Li, *Nat. Commun.*, 2023, **14**, 4491.
51 X. Zhang, X. Zhu, S. Bo, C. Chen, M. Qiu, X. Wei, N. He, C. Xie, W. Chen, J. Zheng, P. Chen, S. P. Jiang, Y. Li, Q. Liu and S. Wang, *Nat. Commun.*, 2022, **13**, 5337.
52 Y. Mao, Y. Jiang, Q. Gou, S. Lv, Z. Song, Y. Jiang, W. Wang, M. Li, L. Zheng, W. Su and R. He, *Appl. Catal., B*, 2024, **340**, 123189.
53 M. Xu, F. Wu, Y. Zhang, Y. Yao, G. Zhu, X. Li, L. Chen, G. Jia, X. Wu, Y. Huang, P. Gao and W. Ye, *Nat. Commun.*, 2023, **14**, 6994.
54 N. Meng, X. Ma, C. Wang, Y. Wang, R. Yang, J. Shao, Y. Huang, Y. Xu, B. Zhang and Y. Yu, *ACS Nano*, 2022, **16**, 9095–9104.
55 N. Cao, Y. Quan, A. Guan, C. Yang, Y. Ji, L. Zhang and G. Zheng, *J. Colloid Interface Sci.*, 2020, **577**, 109–114.
56 H. Wang, Y. Jiang, S. Li, F. Gou, X. Liu, Y. Jiang, W. Luo, W. Shen, R. He and M. Li, *Appl. Catal., B*, 2022, **318**, 121819.
57 C. Lv, L. Zhong, H. Liu, Z. Fang, C. Yan, M. Chen, Y. Kong, C. Lee, D. Liu, S. Li, J. Liu, L. Song, G. Chen, Q. Yan and G. Yu, *Nat. Sustainability*, 2021, **4**, 868–876.
58 S. Fu, K. Chu, M. Guo, Z. Wu, Y. Wang, J. Yang, F. Lai and T. Liu, *Chem. Commun.*, 2023, **59**, 4344–4347.
59 Y. Lum and J. W. Ager, *Nat. Catal.*, 2019, **2**, 86–93.
60 H. Xiao, W. A. Goddard, T. Cheng and Y. Liu, *Proc. Natl. Acad. Sci. U. S. A.*, 2017, **114**, 6685–6688.
61 K. Hadjiivanov, E. Ivanova, M. Daturi, J. Saussey and J. C. Lavalley, *Chem. Phys. Lett.*, 2003, **370**, 712–718.
62 L. Fan, C. Luo, X. Li, F. Lu, H. Qiu and M. Sun, *J. Hazard. Mater.*, 2012, **215–216**, 272–279.
63 P. Roy, A. Pramanik and P. Sarkar, *J. Phys. Chem. Lett.*, 2021, **12**, 10837–10844.
64 X. Zhang, Y. B. Mollamahale, D. Lyu, L. Liang, F. Yu, M. Qing, Y. Du, X. Zhang, Z. Q. Tian and P. K. Shen, *J. Catal.*, 2019, **372**, 245–257.
65 L. Hu, G. Zhan, L. Zhao, J. Dai, X. Zou, J. Wang, W. Hou, H. Li, Y. Yao and L. Zhang, *Adv. Mater.*, 2024, **36**, 2400870.